

# Journal of Hydraulic Research

ISSN: 0022-1686 (Print) 1814-2079 (Online) Journal homepage: <https://www.tandfonline.com/loi/tjhr20>

## Water flow and sediment transport at open-channel confluences: an experimental study

Saiyu Yuan, Hongwu Tang, Yang Xiao, Xuehan Qiu & Yang Xia

To cite this article: Saiyu Yuan, Hongwu Tang, Yang Xiao, Xuehan Qiu & Yang Xia (2018) Water flow and sediment transport at open-channel confluences: an experimental study, *Journal of Hydraulic Research*, 56:3, 333-350, DOI: [10.1080/00221686.2017.1354932](https://doi.org/10.1080/00221686.2017.1354932)

To link to this article: <https://doi.org/10.1080/00221686.2017.1354932>



Published online: 30 Aug 2017.



Submit your article to this journal



Article views: 1422



View related articles



View Crossmark data



Citing articles: 1 View citing articles

Research paper

# Water flow and sediment transport at open-channel confluences: an experimental study

SAIYU YUAN, Assistant Professor, *State Key Laboratory of Hydrology-Water Resources and Hydraulic Engineering, Hohai University, Nanjing, PR China*  
Email: [yuansaiyu@hhu.edu.cn](mailto:yuansaiyu@hhu.edu.cn)

HONGWU TANG, Professor, *State Key Laboratory of Hydrology-Water Resources and Hydraulic Engineering, Hohai University, Nanjing, PR China*  
Email: [\(author for correspondence\)](mailto:hwtang@hhu.edu.cn)

YANG XIAO, Professor, *State Key Laboratory of Hydrology-Water Resources and Hydraulic Engineering, Hohai University, Nanjing, PR China*  
Email: [sediment\\_lab@hhu.edu.cn](mailto:sediment_lab@hhu.edu.cn)

XUEHAN QIU, Engineer, *Shanghai Investigation, Design & Research Institute Co., Ltd., Shanghai, PR China*  
Email: [qiuxuehan@hotmail.com](mailto:qiuxuehan@hotmail.com)

YANG XIA, PhD Student, *State Key Laboratory of Hydrology-Water Resources and Hydraulic Engineering, Hohai University, Nanjing, PR China*  
Email: [xiayang@hhu.edu.cn](mailto:xiayang@hhu.edu.cn)

## ABSTRACT

The knowledge of the dynamics of urban channel confluences is insufficient as most past studies have focused on natural river confluences. This paper reports experimental observations on bed morphology and hydrodynamics of the urban confluences and their dependence to the discharge ratio. Typical hydrodynamic and morphological features such as the shear layer, helical cells, bars and scour holes are identified. Nevertheless, the presence of a region of low-velocity flow for a small discharge ratio differs from results obtained in previous studies. Two sand ridges associated with the corridors of the eroded sediment from the scour holes merge into a mid-stream bar. Results also show that the intense shear towards the bed by downwelling and upwelling flows involved in helical motions is responsible for the mid-stream scour hole.

**Keywords:** Bed morphology; flow structure; helical flow; open-channel confluence; shear layer

## 1 Introduction

Urban channels are usually prismatic or rectangular with a width-to-depth ratio smaller than in natural channels (Arega, Lee, & Tang, 2008; Yuan et al., 2016). Two enjoining urban channels at an urban channel confluence are often of similar dimensions, followed by a wider post-confluence channel. Confluence of flows often results in a downstream shear layer which enhances turbulent mixing. This leads to enhanced exchange of momentum and mass (e.g. sediment and pollutants) across the shear layer. In-depth knowledge of the dynamics of urban confluences is required to mitigate flooding in cities and improve

protection to the environment. Previous studies have primarily focused on the dynamics of river confluences, which exhibit larger width-to-depth ratios. Hereafter, previous studies related to hydraulics, bed morphology and sediment dynamics at river confluences are briefly reviewed, since there are many commonalities between natural rivers and urban channels.

Flow dynamics at channel confluences are characterized by six distinct regions including areas of flow stagnation, flow deflection, flow separation, maximum velocity, gradual flow recovery and shear layers (Best, 1987, 1988). Of particular research interest is the separation zone (e.g. Best & Reid, 1984; Yang, Wang, Lu, & Wang, 2009) and the

Received 12 May 2016; accepted 8 July 2017/Open for discussion until 31 December 2018.

shear layer (e.g. Rhoads & Sukhodolov, 2004, 2008). Helical flow cells, although not included in the previous conceptual models, have been observed in natural (Rhoads & Kenworthy, 1995, 1998; Rhoads, Riley, & Mayer, 2009) and artificial (e.g. Mosley, 1976) confluences and by means of numerical simulations (Bradbrook, Lane, & Richards, 2000; Constantinescu, Miyawaki, Rhoads, & Sukhodolov, 2012; Constantinescu, Miyawaki, Rhoads, Sukhodolov, & Kirkil, 2011). Twin surface-convergent helical cells are observed on either side of the shear layer in the vertical plane and can rapidly evolve into a single, channel-width circulation cell due to the difference in the curvature of the two combining flows (Bradbrook, Lane, & Richards, 2000; Rhoads & Kenworthy, 1995, 1998).

The shear layer is characterized by increased turbulence levels and it is a common occurrence at channel confluences (Biron, Roy, & Best, 1996b; Bradbrook, Lane, Richards, Biron, & Roy, 2000), where there is a significant velocity gradient between the two combining flows. Rhoads and Sukhodolov (2004) pointed out that the eddy development process in the shear layer in the horizontal plane was similar to traditional vortex pairing. These quasi-two-dimensional vortices with near-vertical axes can lead to substantial lateral transfer of fluid between the two combining flows (Rhoads & Sukhodolov, 2001; Sukhodolov & Rhoads, 2001). Constantinescu et al. (2012) showed that the types of coherent structures could be affected by the discharge ratio. When the discharges of the two rivers were comparable, the shear layer was populated by quasi two-dimensional eddies with opposing sense of rotation; otherwise, the shear layer contained predominantly corotating large-scale quasi two-dimensional eddies whose growth was driven by the Kelvin–Helmholtz instability and vortex pairing.

The shear layer does not always have a two-dimensional nature. Bed discordance, which is defined as the difference in bed elevation between two channels, can result in the distortion of the shear layer and consequently the upwelling of water at the downstream junction corner (Biron, Roy, & Best, 1996a, 1996b; Bradbrook, Lane, Richards, Biron, & Roy, 2001; De Serres, Roy, Biron, & Best, 1999), and can affect bed morphology and sedimentology (Biron, Roy, Best, & Boyer, 1993; Boyer, Roy, & Best, 2006). The large lateral advection of the mean flow associated with helical motions can also result in the distortion of the shear layer (Rhoads & Sukhodolov, 2008), particularly at urban channel confluences (Yuan et al., 2016). Yuan et al. (2016) showed that the flow turbulence structure at urban channel confluences with a distorted shear layer could result in the redistribution of the maximum turbulent kinetic energy, Reynolds shear stress and ejection and sweep events. However, the hydromorphodynamics at urban channel confluences, particularly those confluences with a large discharge from the tributary, remain largely unexplored.

Principal morphological features have been identified at river confluences, including a scour hole, bank-attached lateral bars, tributary-mouth bars, and a region of sediment accumulation near the upstream confluence corner (Best, 1988). Despite

numerous field surveys (Biron et al., 1993; Boyer et al., 2006; Rhoads et al., 2009) and laboratory experiments (Best, 1988; Guillén-Ludeña, Franca, Cardoso, & Schleiss, 2015, 2016; Leite Ribeiro, Blanckaert, Roy, & Schleiss, 2012) on sediment transport and morphology at river confluences, the interaction between flow dynamics and bed morphology remains poorly understood due to the complex erosion and deposition processes at river confluences (Guillén-Ludeña et al., 2015). Many hypotheses have been proposed for the origin of the mid-stream scour hole, such as the large flow velocity, strong turbulence, the effect of the shear layer or the curvature-induced helical circulation (Best, 1988; Guillén-Ludeña et al., 2015, 2016; Leite Ribeiro et al., 2012; Rhoads et al., 2009; Sukhodolov & Rhoads, 2001).

The principal objective of the present study was to investigate the dynamics of urban channel confluences by presenting a detailed analysis of the bed morphology and flow dynamics in a laboratory confluence with two different discharge ratios. In addition, a general process-response model of the hydro-morpho-sedimentary processes is proposed. It is important to note that our study differs from previous studies in three important aspects: (1) the width-to-depth ratio of both main channel and tributary is close to 2, which is considerably smaller than that of rivers and that in previous studies; (2) the width of the post-confluence channel is about 1.4 times that of the main channel and tributary, as the channel width scales with the flow rate  $B \propto Q^{0.5}$ , where  $B$  is the width and  $Q$  is the discharge (Ferguson & Hoey, 2008); and (3) we explored the probable causes for the formation of the mid-channel scour hole at urban channel confluences.

The remainder of this paper is structured as follows. In Section 2, we introduce the experimental set-up and the channel confluences. In Sections 3 and 4, we analyse flow, morphology, and sediment transport processes in the laboratory experiment. In Section 5, we discuss the hydro-morpho-sedimentary processes at urban channel confluence, which were compared with previous studies.

## 2 Experimental methods

The experimental set-up used in this study is not a scale model of a particular confluence, but rather a schematized configuration that aims to simulate the dominant flow structures and sedimentary processes in a broader range of configurations, as shown in Fig. 1. The straight upstream channel is concordant with a width of 30 cm and a length of 3 m each, while the confluent channel is slightly wider (40 cm) and longer (7 m). The junction angle is 90°. Water is pumped from the downstream tank to the two upstream tanks through 110-mm-diameter PVC pipes, and flow discharges are strictly controlled by two ultrasonic flow meters and pump-valve systems. Honeycombs and sufficiently long channels are used to ensure fully developed flows entering the junction point. The water level is adjusted

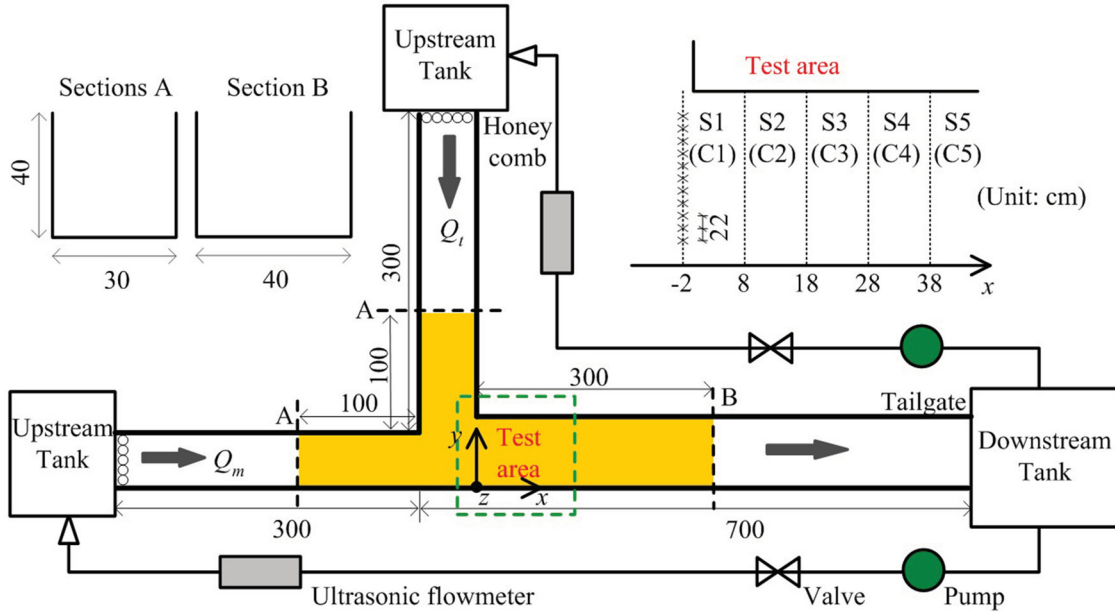


Figure 1 Sketch of the experimental set-up: A 90° confluence channel flume with horizontal erodible sand bed (not to scale) and the cross sections for measurement

Table 1 Hydraulic data of experiment

Case no.	$h$ (m)	$Q_m$ ( $\text{l s}^{-1}$ )	$Q_t$ ( $\text{l s}^{-1}$ )	$\gamma$	$F_m$	$F_t$	$F_{pc}$	$R_m$	$R_t$	$R_{pc}$
1	0.165	9	6	0.4	0.14	0.10	0.18	14,144	9430	20,344
2	0.165	6	9	0.6	0.10	0.14	0.18	9430	14,144	20,344

Note:  $h$  is the water depth;  $Q$  is the discharge;  $F$  and  $R$  are the Froude number and the Reynolds number after the quasi-equilibrium stage. The subscripts “ $m$ ”, “ $t$ ” and “ $pc$ ” represent the main channel, the tributary and the post-confluence, respectively;  $\gamma$  is the discharge ratio calculated by  $Q_t/(Q_t + Q_m)$ .

by the tailgate downstream. All channels have a rectangular cross section and a flat bottom. The reference axes ( $x$ ,  $y$ ,  $z$ ) are shown in Fig. 1. The discharge ratio is defined as the ratio of the tributary discharge to the total discharge of the two upstream channels, and two discharge ratios (0.4 and 0.6) are considered in this study (Table 1). Hydraulic conditions of this type of experiment, such as the Froude number, can vary during the evolution of the morphology (Guillén-Ludeña et al., 2015). Hence, these conditions after the bed morphology developing up to the quasi-equilibrium stage (Kumar & Kothiyari, 2012) are listed in Table 1. The confluent channels with such hydraulic conditions are common in urban drainage networks in eastern China.

Both tests were conducted under clear-water conditions, i.e. no suspended or bed load was added. The bed was initially covered with a layer of sediment. The sediment used in this study satisfied the following requirements: (1) the amount of sediment entrained in the two upstream channels and in the downstream flow recovery zone was not large; (2) scour holes and bars at the confluence hydrodynamic zone (CHZ) formed to create a typical bed morphology; (3) the bed was armoured after the erosion of fine sediment. The cross-sectional mean velocity in the flow-recovery zone was about  $0.227 \text{ m s}^{-1}$ , and the corresponding

grain size for sediment entrainment was about 0.3 mm according to Vanoni (1975). Hence, poorly sorted sediment was used as the bed material, where  $d_{50} = 0.9 \text{ mm}$ ,  $d_{90} = 2.5 \text{ mm}$ , and the sorting coefficient was  $\sigma = 0.5(d_{84}/d_{50} + d_{50}/d_{16}) = 2.41$ . As  $d_{50}$  is much larger than 0.3 mm, there will be little sediment entrainment in the downstream flow recovery zone. Also, negligible sediment entrainment will take place in the two upstream channels, since the velocities in the two channels are smaller than the post-confluence channel.

The bed was initially covered with a 5.5-cm-thick layer of poorly sorted sediment mixture, as shown in the yellow zone in Fig. 1. In addition, the bed was flattened prior to the experiment. Steady flow discharges were provided to the main channel and tributary, respectively. Fine sands were more likely to be eroded by the flow, thus forming a coarser layer to prevent further erosion of beneath finer sands. The quasi-equilibrium stage was determined based on the change in bed morphology, which was obtained about three hours after the beginning of the experiment in this study. The scour holes developed very rapidly, but it took about two weeks to measure velocities. To prevent the evolution of scour holes during velocity measurement, the method of bed fixing suggested by Liriano, Day, and White (2002) was used.

Degraded bed elevation in the zones where sediment erosion and deposition mainly occurred ( $-15 \text{ cm} < x < 80 \text{ cm}$ ) was measured using a laser range finder with an accuracy of 0.1 mm. Three-dimensional flow velocities in the CHZ were measured using an acoustic Doppler velocimeter at a sampling frequency of 100 Hz (ADV, NorTek Vectrino +, Oslo, Norway; maximum velocity:  $4 \text{ m s}^{-1}$ ; accuracy:  $\pm 10^{-3} \text{ m s}^{-1}$ ). Seeding materials consisting of neutrally buoyant hollow glass spheres (Potter Industries Sphericell, Valley Forge, USA) were added to provide acoustic scattering signals for ADV during the tests. Velocities were measured in five cross sections (S1 to S5 for case one and C1 to C5 for case two) perpendicular to the flume walls

in each case (Fig. 1). The transverse spacing of the measured profiles was 2 cm. The interval between two adjacent vertical measurement points near the bed was 0.5 cm, and five points was measured. Above these points, the interval between two adjacent vertical measurement points was expanded to 1 cm.

### 3 Bed morphology and sediment transport

Figure 2 shows the bed elevation contours for the two cases. Two well-developed deep scour holes and a bank-attached lateral bar immediately downstream of the confluence are observed

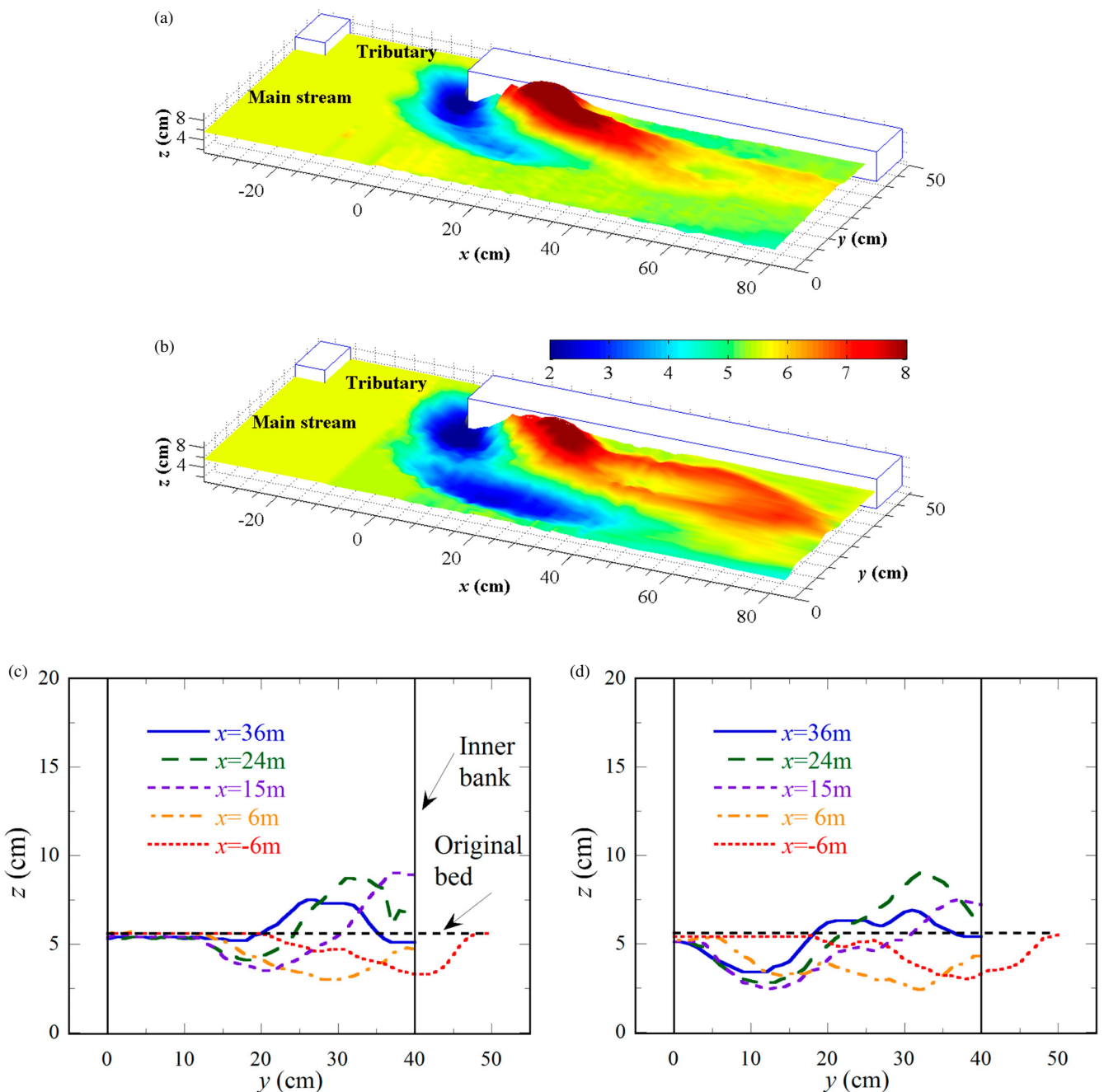


Figure 2 Contours for the degraded beds within the confluence zone (units: cm): (a)  $\gamma = 0.4$  and (b)  $\gamma = 0.6$ ; and the degraded beds of five representative cross sections: (c)  $\gamma = 0.4$  and (d)  $\gamma = 0.6$

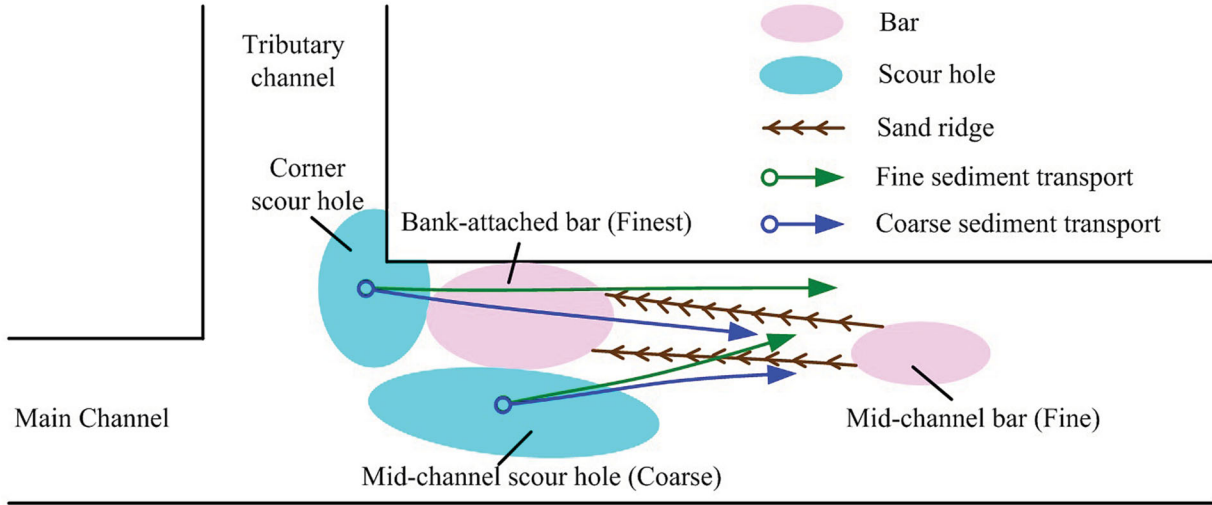


Figure 3 Illustration of bed morphology and sediment transport

in both cases. The scour hole at the corner is developed by the deflection of the tributary flow, and its morphology is less affected by the discharge ratio; while the morphology of the other scour hole is significantly affected by the discharge ratio, and it is related to the confluence hydrodynamics. When the discharge ratio  $\gamma = 0.4$ , it is about 25 cm long and 10 cm wide (where the erosion is larger than 1.2 cm), and has a maximum depth of 2 cm (Fig. 2c); and when  $\gamma = 0.6$ , it is about 45 cm long and 20 cm wide, and has a maximum depth of 3.1 cm (Fig. 2d). Obviously, the increase in the dimensions of the scour hole is related to the increasing tributary flow into the confluence at a higher discharge ratio. The thalweg of the scour hole tends to be parallel to the bank when the discharge ratio is large (Fig. 2b and d). A bank-attached lateral bar is promoted by the reduced pressure and recirculating flow in the flow separation zone due to the flow detachment from the inner wall in the post-confluence channel and its reattachment further downstream, which is also significantly affected by the discharge ratio. The elevation and shape of the bar are similar in two cases, as the sediment originates from the corner scour hole in both cases. Further downstream, the height of the bar decreases, and two sand ridges form with the maximum height at some distance from the inner bank, leading to the formation of two small depressions adjacent to the inner bank and between the two sand ridges that corresponds to the corridors of fine sediment transport, respectively.

The sediment eroded from the corner scour hole is transported along the outer face of the inner ridge, and finer sediment can pass over the ridge and is transported along the inner corridor (Fig. 3). The sediment eroded from the mid-stream scour hole is conveyed along the outer face of the outer ridge. Similarly, the finer sediment can also pass over the ridge and is then transported between the two ridges (Fig. 3). The two sand ridges are merged at  $x = 65$  cm, where a mid-channel bar is formed because the flow velocities and turbulence intensities decrease as the shear layer dissipates (Rhoads & Sukhodolov,

2004; Sukhodolov & Rhoads, 2001). According to the elevation variation, the total volume of sediment eroded is  $385 \text{ cm}^3$  in case one and  $107 \text{ cm}^3$  in case two, respectively. Therefore, although the bed morphology is more pronounced with a deeper mid-channel scour hole in case two, most sediment eroded from the two scour holes can settle down to form bars and sand ridges, resulting from the larger region of separation flow. The grain sorting of surface samples in case one is further illustrated by means of the grain size distribution (Fig. 4a) in the erosion zone (A1), the deposition zone (A2) and the post-confluence mid-channel bar (A3). Compared with the input sediment ( $d_{50} = 0.9 \text{ mm}$ ), sediment at A2 ( $d_{50} = 0.46 \text{ mm}$ ) and A3 ( $d_{50} = 0.48 \text{ mm}$ ) is finer; while that at A1 ( $d_{50} = 1.4 \text{ mm}$ ) is coarser. Figure 4b shows that the input sediment is poorly sorted, and the sediment in the ranges of  $0.355\text{--}0.5 \text{ mm}$  and  $1.4\text{--}3 \text{ mm}$  accounts for about 85% of the total amount. The deposition and erosion of fine sediment result in a high percentage of fine grains at A2 and a high percentage of coarse grains at A1, respectively. During the transport of sediment along the ridges, coarse sediment can settle down due to flow recovery and form the mid-stream bar. Hence, the sediment at A3 is coarser than that at A2.

## 4 Flow dynamics

### 4.1 Collection and analysis of velocity data

The test areas and measurement points are marked in Fig. 1. Three-dimensional velocities in the confluence zone were measured using an ADV at a sampling frequency of 100 Hz over a period of 120 s. Figure 5a and b give an example of the time series of the three-dimensional velocities. Raw data of streamwise velocity, cross-stream velocity and vertical velocity were processed by removing weak signals ( $< 30$  signal-to-noise ratio), poorly correlated signals ( $< 90\%$  correlation) and despiking using the phase-space threshold method proposed by Goring

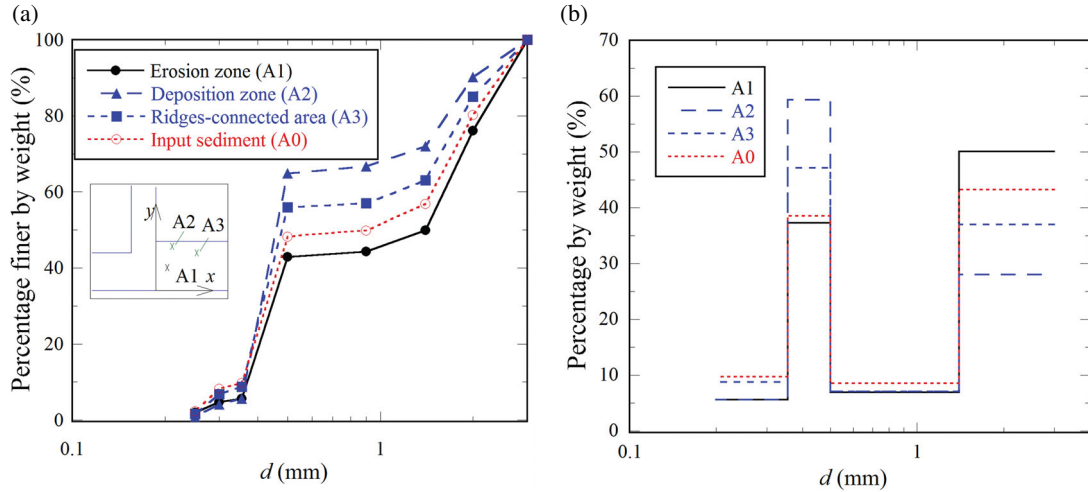


Figure 4 Grain size distribution of samples measured by hand sieving (a) and mass fraction of a certain grain size range of surface sediment in case one (b)

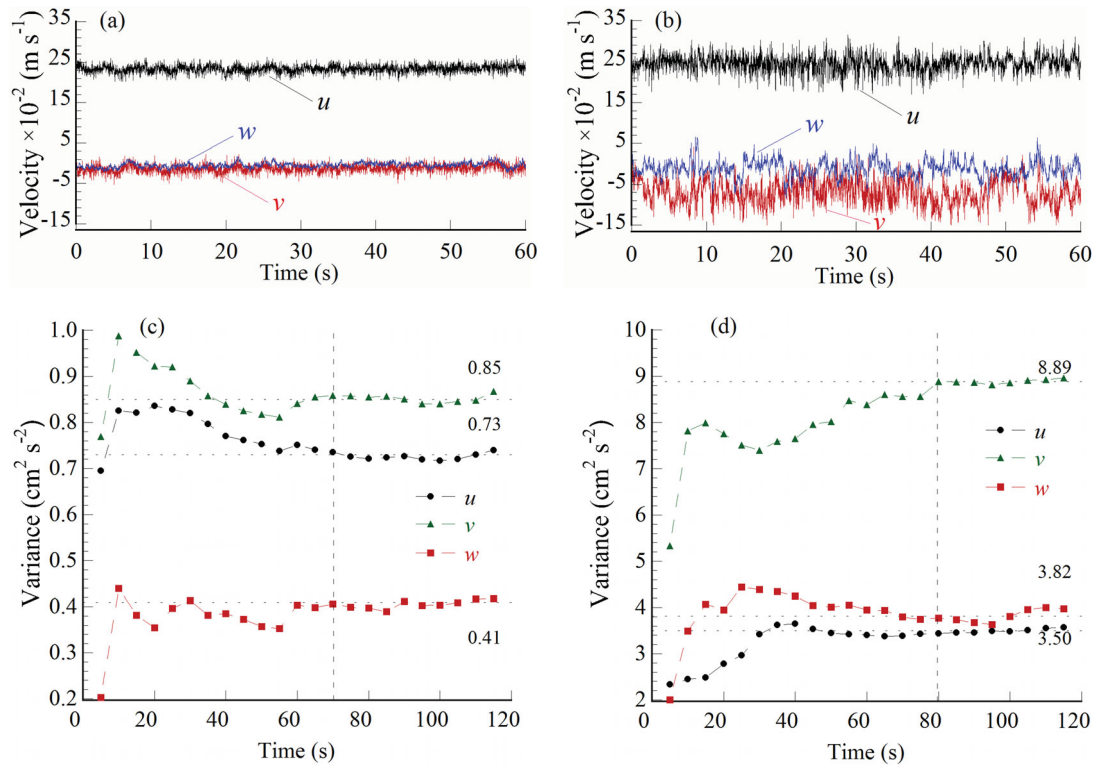


Figure 5 Examples of time series and stationarity analysis of three dimensional velocities,  $u$ ,  $v$ , and  $w$ , near the water surface (a, c) outside the shear layer ( $y = 11.5 \text{ cm}$ ,  $z = 13.2 \text{ cm}$ ) and (b, d) within the shear layer ( $y = 19.5 \text{ cm}$ ,  $z = 12.1 \text{ cm}$ ) in C2

and Nikora (2002) (Yuan, Li, Amini, & Tang, 2014). The accuracy of estimates of the time-averaged flow velocities using an acoustic Doppler instrument is typically better than 4% (Lemmin & Rolland, 1997; Rolland, 1994). The Doppler noise of the different receivers is statistically independent, which suggests that the estimates of the turbulent shear stresses are noise-free. The noise mainly biases the turbulent normal stresses and turbulent kinetic energy, and may cause the uncertainty of about 20% (Blanckaert, 2010).

The stationarity analysis involved dividing each time series into 24 intervals of equal length and then progressively

cumulating the variance over these 24 intervals (Fig. 5c and d). The systematic convergence of the cumulative variance on a constant value is indicative of a stationary variance, suggesting that the record length is sufficient to capture the major sources of variation in velocity. The plots for the strong- and weak-turbulent flow (indicated by the turbulent kinetic energy  $k$  in Section 4.3) exhibit convergence, and the record length is defined to be equal to 90% of the long-term mean variance. These values, which serve as sampling intervals for flow measurements, are 70 s for the weak-turbulent flow and 80 s for the strong-turbulent flow (Fig. 5c and d).

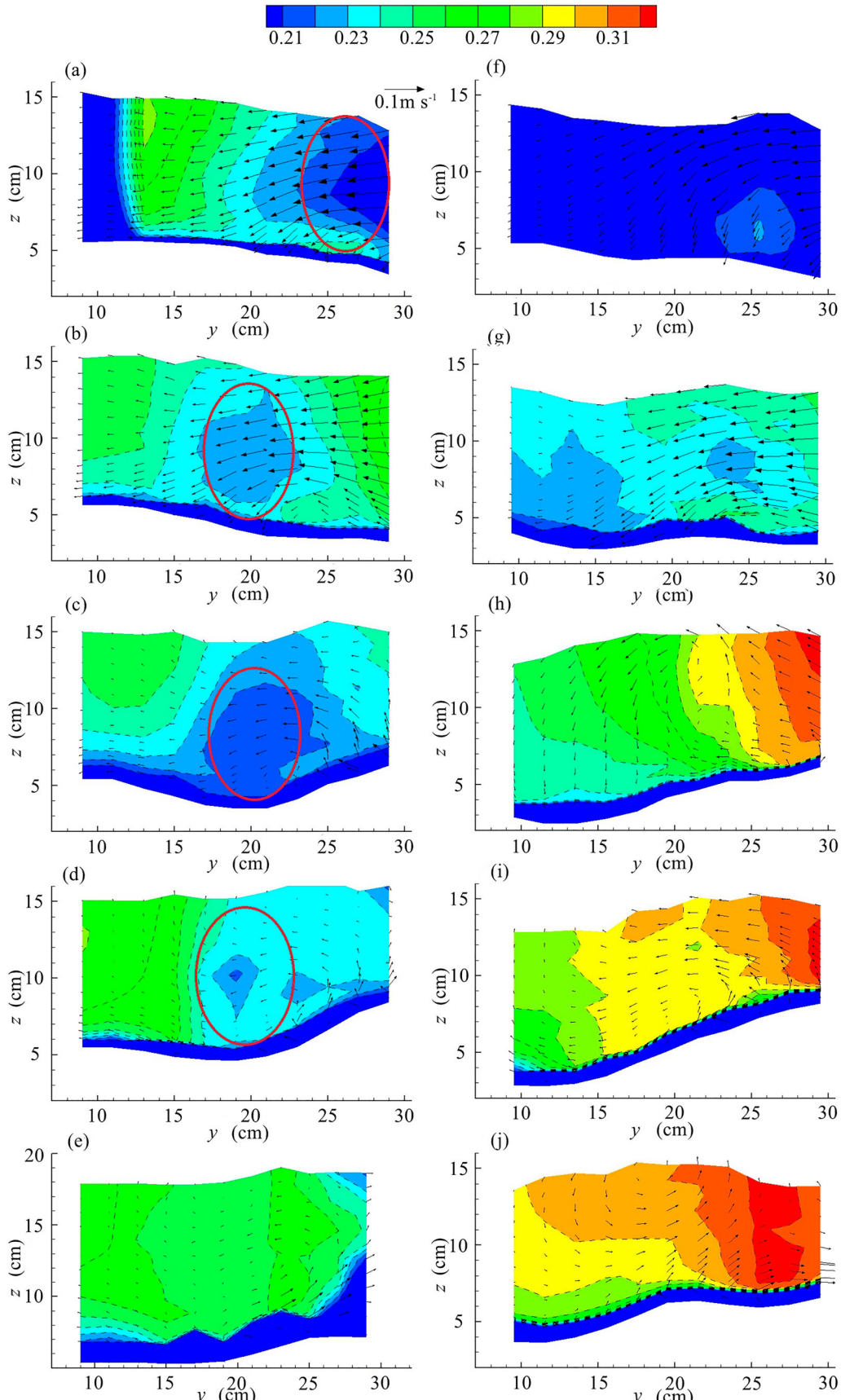


Figure 6 Patterns of time-averaged streamwise flow velocity  $u$  (contours, units:  $\text{m s}^{-1}$ ) and cross-sectional velocities,  $v$ ,  $w$  (vectors) of two cases, with (a–e) representing five cross sections S1–S5, respectively; and (f–j) representing C1–C5, respectively. The red ovals represent the region of low-velocity flow

#### 4.2 Three-dimensional velocity field

Figure 6 plots the vectors of the cross-sectional velocities ( $v, w$ ) superimposed on the contours of the streamwise velocities  $u$  for the two cases using *Tecplot 360®*, Bellevue, USA, where  $u, v$  and  $w$  are the three components of flow velocity in the reference axes,  $x, y$  and  $z$ , respectively. The penetration of the tributary flow causes considerable redistribution of the main channel flow. As a result, in case one, the flow velocity originating from the main channel is increased from  $0.18 \text{ m s}^{-1}$  in S1 to  $> 0.27 \text{ m s}^{-1}$  in S5 near the outer bank; and the streamwise velocity in the inner side (except the region of flow separation) is also increased from  $0.21 \text{ m s}^{-1}$  in S1 to  $0.26 \text{ m s}^{-1}$  in S5. Interestingly, a region of low-velocity flow can be clearly observed in S2 and the other downstream cross sections, which has not been described in the conceptual model proposed by Best (1987) and Leite Ribeiro et al. (2012). Although the flows originating from the tributary are accelerated by the squeeze of the main channel flow and the separation flow, the widening of the post-confluence channel results in a decrease in the intensity of the squeeze and makes their velocities still smaller than the main channel. This zone is mainly distributed at around  $y/B_{pc} = 0.5$ , and moves slightly outward from S1 to S5. A nearly unidirectional outward flow is observed in S1 and S2; while helical flow can be distinguished in the following three cross sections. For in-depth analysis of the helical motions by the Rozovskii method refer to Rhoads and Kenworthy (1998); this is not discussed here. It is interesting that the strong downwelling flow (induced by helical motions and the blockage of the flow from the main channel) is observed in the deepest part of the scour hole and the upwelling flow along the face of the bank-attached bar. This helical cell is centred at the original bed surface ( $z/h = 0.33$ ) in S3 and gradually rises to the middle of the water depth ( $z/h = 0.76$ ) in S5, caused by the rising bed elevation and the development of helical cell.

In case two, the penetration of the tributary flow also results in an increase in the streamwise velocity from  $0.18 \text{ m s}^{-1}$  to  $0.30 \text{ m s}^{-1}$  near the outer bank, and an increase from  $0.19 \text{ m s}^{-1}$  to  $0.32 \text{ m s}^{-1}$  near the inner bank except the region of flow separation. It is noted that the increase in velocity is more pronounced than that in case one, since there is a larger region of flow separation to narrow the path for the two combined flows. However, the region of low-velocity flow is not observed in this case. The streamwise velocities decrease with transverse distance from the region of flow separation. A nearly unidirectional outward flow is observed in C1 and C2. Because of the blockage of the flow originating from the main channel, a strong downwelling flow is noted at the deepest part of the scour hole ( $y/B_{pc} = 0.33$ ) in C3. An anticlockwise helical cell occurs and develops from C4 to C5, and rapidly rises to near the water surface ( $z = 15 \text{ cm}$ ) probably due to the highly bulged bed morphology. We can infer that sediment at the scour hole may be eroded as a result of the intense shear toward the bed by the downwelling flow and conveyed along the outer face of the

outer ridge by the helical flow, according to an upward obliquely narrow groove observed on the face of the bar which indicates the path of sediment transport.

#### 4.3 Kinetic energy of turbulence

The strong turbulence in the CHZ, characterized by scales of eddies and vortices and identified by large turbulent kinetic energy, lies in the regions of the shear layer, helical flow cells, flow separation and near the boundary named wall turbulence. The turbulent kinetic energy is calculated as the sum of the intensity of velocity fluctuations:

$$k = 0.5 \sum_{i=1}^3 \langle u_i'^2 \rangle \quad (1)$$

where  $k$  is the turbulent kinetic energy, and  $\langle u_i'^2 \rangle$  ( $i = 1, 2, 3$ ) represents the turbulent kinetic energy of each component of the fluctuating velocity,  $u'$ ,  $v'$ , and  $w'$ , which can be calculated as:

$$\langle u_i'^2 \rangle = \text{var}(u_i) = \frac{1}{n} \sum_{j=1}^n (u_i - \langle u_i \rangle)^2 \quad (2)$$

where  $u_i$  is the component of velocity,  $u, v$  and  $w$  ( $i = 1, 2$ , or 3), and their mean values are represented as  $\langle u_i \rangle$ ,  $\text{var}()$  represents the variance, and  $n$  is the number of velocity data.

The distribution of turbulent kinetic energy within the cross sections shows the time-averaged turbulence structure in the CHZ, and the shear layer is characterized by the increased turbulence level (Fig. 7; Sukhodolov & Rhoads, 2001). The shear layer weakens considerably with longitudinal distance from the junction point. In case one, the shear layer could be distinguished by a vertical band with large values of  $k$  in the upstream two cross sections, whose centre is at about  $y/B_{pc} = 0.52$  in S1 and  $y/B_{pc} = 0.48$  in S2, respectively. This band expands downstream and weakens considerably, which is indicated by the attenuated transverse gradient in the near surface velocities (Fig. 6). There is almost no transverse velocity gradient in S5, indicating the recovery of the flow (Fig. 6), and thus the band which indicates the shear layer disappears. The red core of the maximum  $k$  values near the inner bank indicates the helical motions, and it coincides with the helical cells observed in Fig. 6. The maximum values of  $k$  decrease from S1 to S3 and then increase in S4 which shall be related to the bulged bed morphology in S4. The strong turbulence of the helical flows above the bar slope shall play an important role in sediment transport. The strong turbulence near the bed surface in the outer bank is induced by the bottom friction, which is termed “wall turbulence”. The strong turbulence near the inner bank (upper portion in S3 and S4 and inner portion in S5) illustrates the flow recirculation in the region of flow separation.

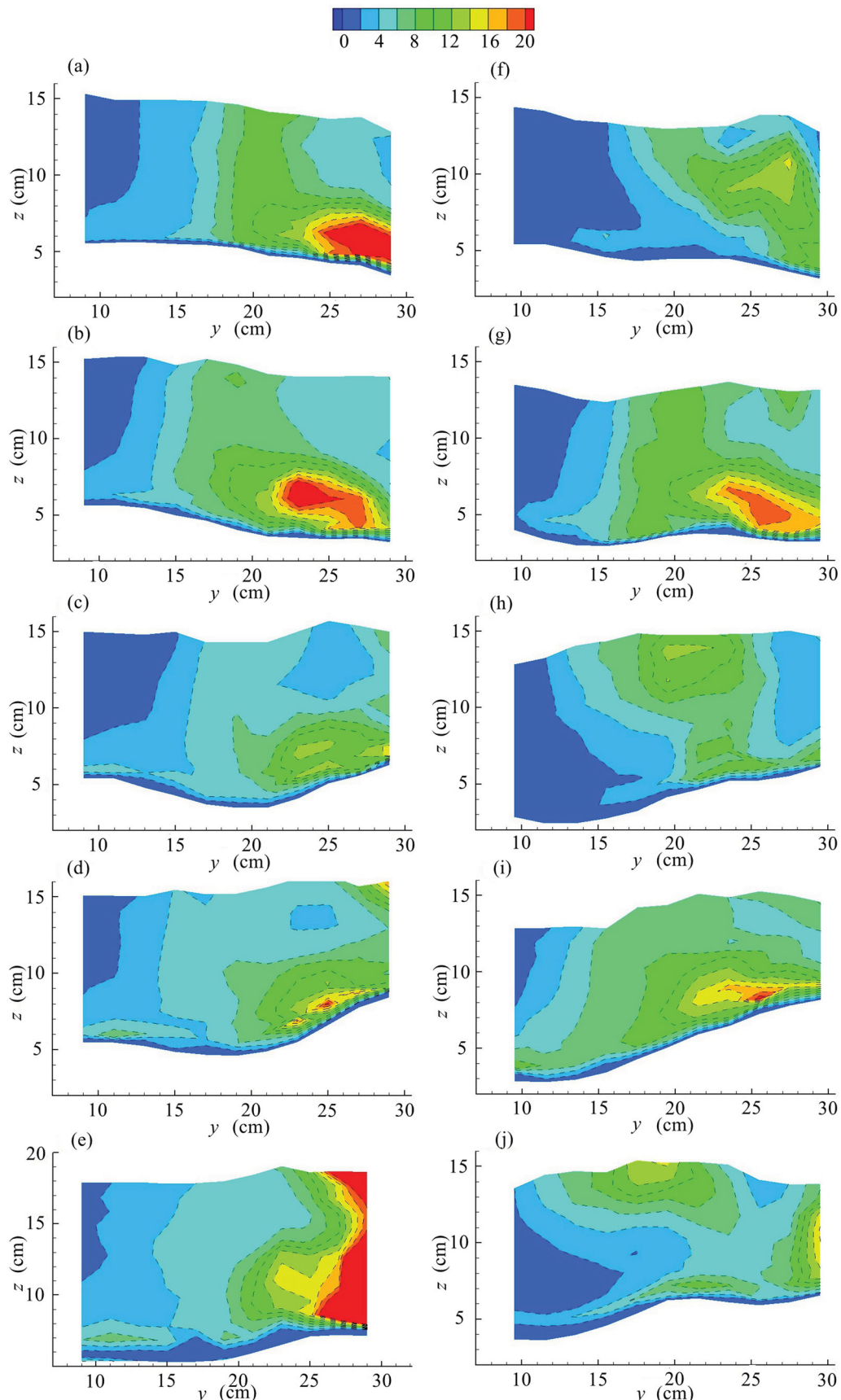


Figure 7 Patterns of turbulent kinetic energy  $k$  (units:  $\text{cm}^2 \text{ s}^{-2}$ ) of two cases (Table 1), with (a–e) representing five cross sections S1–S5, respectively; and (f–j) representing C1–C5, respectively

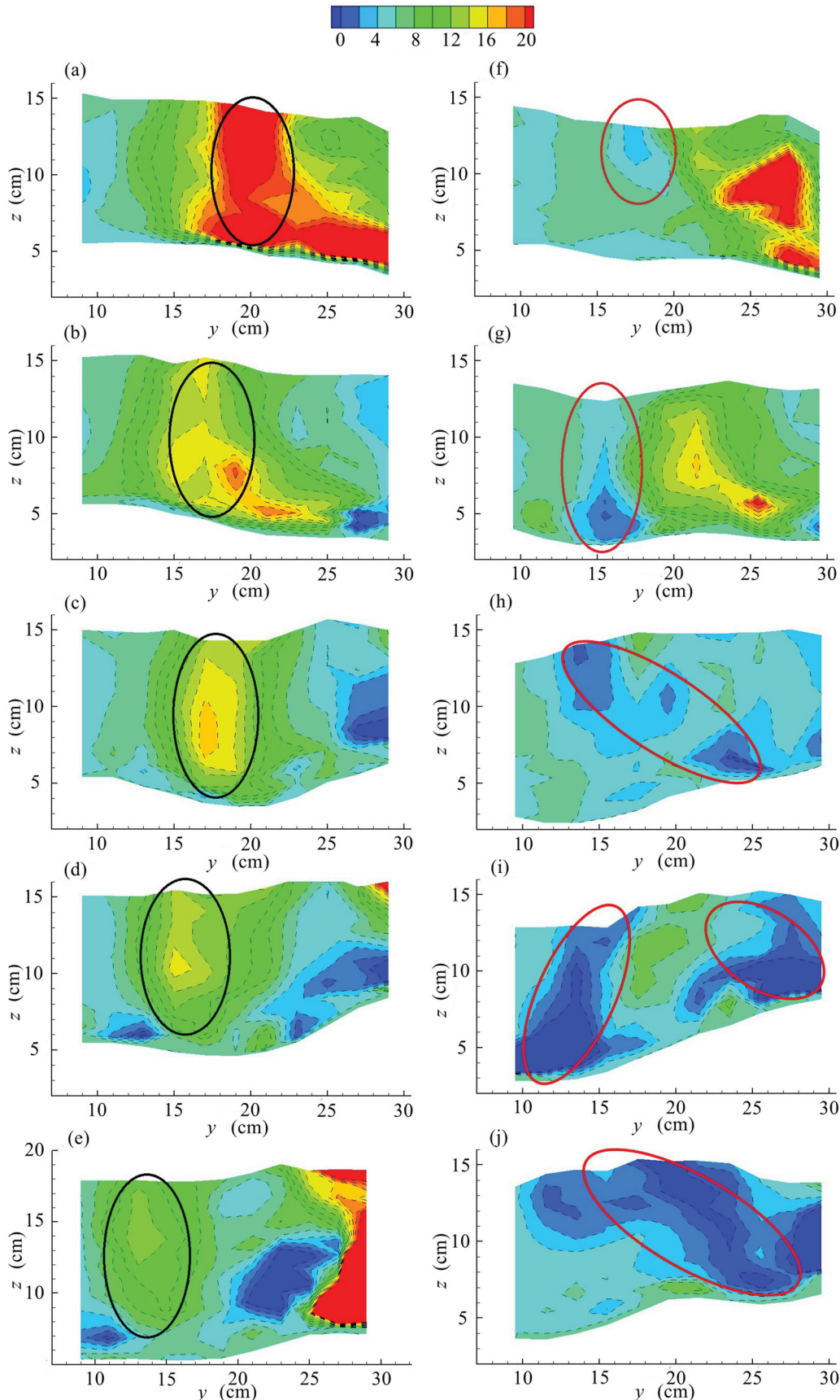


Figure 8 Patterns of the Reynolds shear stress  $\langle u'v' \rangle$  (units:  $\text{cm}^2 \text{s}^{-2}$ ) of two cases (Table 1), with (a–e) representing five cross sections S1–S5, respectively; and (f–j) representing C1–C5, respectively

In case two, the shear layer indicated by large values of  $k$  tends to be distorted in S3 and S5, which is common at open-channel confluences with a small width-to-depth ratio and a large discharge ratio (Yuan et al., 2016). The distortion of the shear layer is expected due to the highly inclined transverse gradient of flow velocities (Fig. 6). This is particularly pronounced in S4, which is probably caused by the highly bulged bed morphology. The helical motions can be identified by the maximum values of  $k$  in C4. The similar features of wall turbulence and flow circulation can also be discerned in case two. The relationship between the scour hole and the strong turbulence proposed in previous studies (e.g. Best, 1987) may be inapplicable for urban channel confluences with a small width-to-depth ratio and a large discharge ratio, since there is no strong turbulence on the scour hole in C3 and C5. The large turbulence on the bar slope may have a more significant effect on the development of the mid-stream scour hole.

#### 4.4 Reynolds stresses

The distribution of the Reynolds stress ( $-\rho \langle u'_i u'_j \rangle$ ) indicates the correlations between velocity components,  $u'_i$  and  $u'_j$ , and reflects the time-averaged vortices or eddies in the  $i-j$  plane. For simplicity,  $\langle u'_i u'_j \rangle$  is used to represent the Reynolds stress. It can be calculated as the covariance of  $u_i$  and  $u_j$ .

Figure 8 plots the contours for the Reynolds shear stress  $\langle u'v' \rangle$  in the two cases. The shear layer with large-scale rotational motions in the horizontal plane could be delineated by the regions with large values of  $\langle u'v' \rangle$ , as the shear layer involves quasi-two-dimensional vortices with near vertical axes between the two combining flows (Rhoads & Sukhodolov, 2001; Sukhodolov & Rhoads, 2001). In case one, the band with large positive values of  $\langle u'v' \rangle$  in S1 is vertically located near  $y/B_{pc} = 0.51$ , and gradually moves to the outer bank near  $y/B_{pc} = 0.41$  in S5; and their values decrease considerably from  $> 2.0 \text{ cm}^2 \text{ s}^{-2}$  in S1 to  $0.8 \text{ cm}^2 \text{ s}^{-2}$  in S5. However, it is noteworthy that the core does not coincide exactly with the deepest scour hole with a deviation of about 3 cm in S3 and S4. Compared with the turbulent kinetic energy which is affected by the cross-sectional helical flow cells on the bar slope, Reynolds shear stress  $\langle u'v' \rangle$  performs better in locating the shear layer. The red core near the inner bank (the upper zone in S3 and S4 and the inner zone in S5) indicates the strong horizontal recirculation in the region of flow separation. In case two, the negative values of  $\langle u'v' \rangle$  are associated with the clockwise (from the top view) horizontal motions and indicate the location of the shear layer, which is consistent with the transverse gradient of flow velocities in Fig. 6. The absolute values of  $\langle u'v' \rangle$  in the cores increase from  $0.2 \text{ cm}^2 \text{ s}^{-2}$  in C1 to  $> 0.8 \text{ cm}^2 \text{ s}^{-2}$  in C5, which is completely different from that in case one. This is because the water depth decreases and the flow from the tributary accelerates due to the highly bulged bank-attached bar, resulting in a more pronounced transverse gradient of flow velocities. There are two heavily inclined bands with large values of  $\langle u'v' \rangle$  in C3

and C5, which corroborates the distorted shear layer (Yuan et al., 2016). The bulged bed surface cuts the inclined band into two parts in C3, and this is more obvious in C4 with one part at the deep scour hole and the other part near the inner bank. However, these two parts are merged into a single inclined band in C5. The red cores in C1 and C2 illustrate the horizontal deflection of the flow originating from the tributary. As mentioned in Section 4.3, the location of the shear layer is not consistent with the scour hole and shall not be related to the formation of scour hole.

Figure 9 shows the contours for the Reynolds shear stress  $\langle u'w' \rangle$  in the two cases. In case one, the large negative values of  $\langle u'w' \rangle$  producing positive shear stresses ( $-\rho \langle u'w' \rangle$ ) are mainly located near the bottom at the outer side, and are associated with wall turbulence. The band with large positive values of  $\langle u'w' \rangle$  is nearly coincident with the location of the deep scour hole and the zone of low-velocity flow in Fig. 6, and the inner edge of the shear layer as indicated by  $\langle u'v' \rangle$  (Fig. 8). The values of  $\langle u'w' \rangle$  decrease gradually with distance from the junction point due to the dissipation of the shear layer, as Yuan et al. (2016) linked the observed positive values of  $\langle u'w' \rangle$  within the shear layer to the near-bed distortion of the shear layer characterized by clockwise vortices from a top view. In case two, the similar cores are also observed in the first two cross sections, which might be related to the deflection of the flow originating from the tributary. The band with large negative values of  $\langle u'w' \rangle$  is nearly coincident with the shear layer (Fig. 8) from C3 to C5. Yuan et al. (2016) also observed negative values of horizontal–vertical cross stresses due to the inclined vortices within the distorted shear layer, which was characterized by anticlockwise vortices from a top view when the discharge of the tributary was large.

Figure 10 shows the contours for the Reynolds shear stress  $\langle v'w' \rangle$  in the two cases. In case one, the large negative values of  $\langle v'w' \rangle$  are mainly located above the scour hole and the avalanche face of the bank-attached bar, which coincident with the location of the helical cells in Fig. 7. The values of  $\langle v'w' \rangle$  remain almost constant with increasing distance from the junction point, which is also coincident with the almost constant intensity of helical motions (Fig. 7). In case two, the similar red cores are also observed, which are also consistent with the location of the helical motions as indicated in Fig. 7. The values of  $\langle v'w' \rangle$  in five cross sections are very different which shall be attributed to the influence of the highly bulged bed morphology as mentioned in Section 4.2.

## 5 Discussion of hydro-morpho-sedimentary processes

In previous sections, we analysed the bed morphology, sediment transport and flow dynamics at channel confluences separately. In this section, we attempt to integrate these results into a conceptual hydro-morpho-sedimentary model for urban channel confluences, and compare these results with previous studies

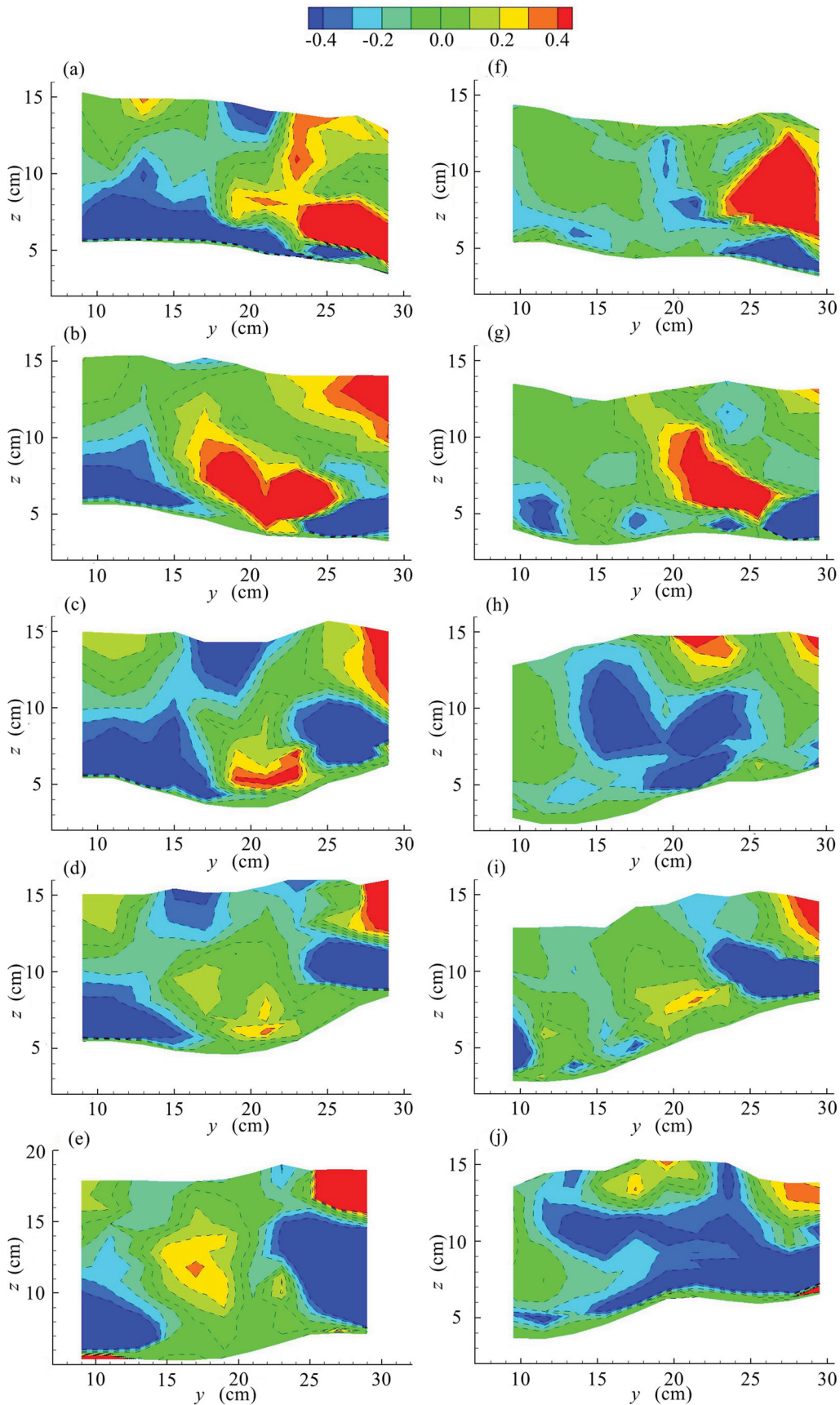


Figure 9 Patterns of the Reynolds shear stress  $\langle u'w' \rangle$  (units:  $\text{cm}^2 \text{s}^{-2}$ ) of two cases (Table 1), with (a–e) representing five cross sections S1–S5, respectively; and (f–j) representing C1–C5, respectively

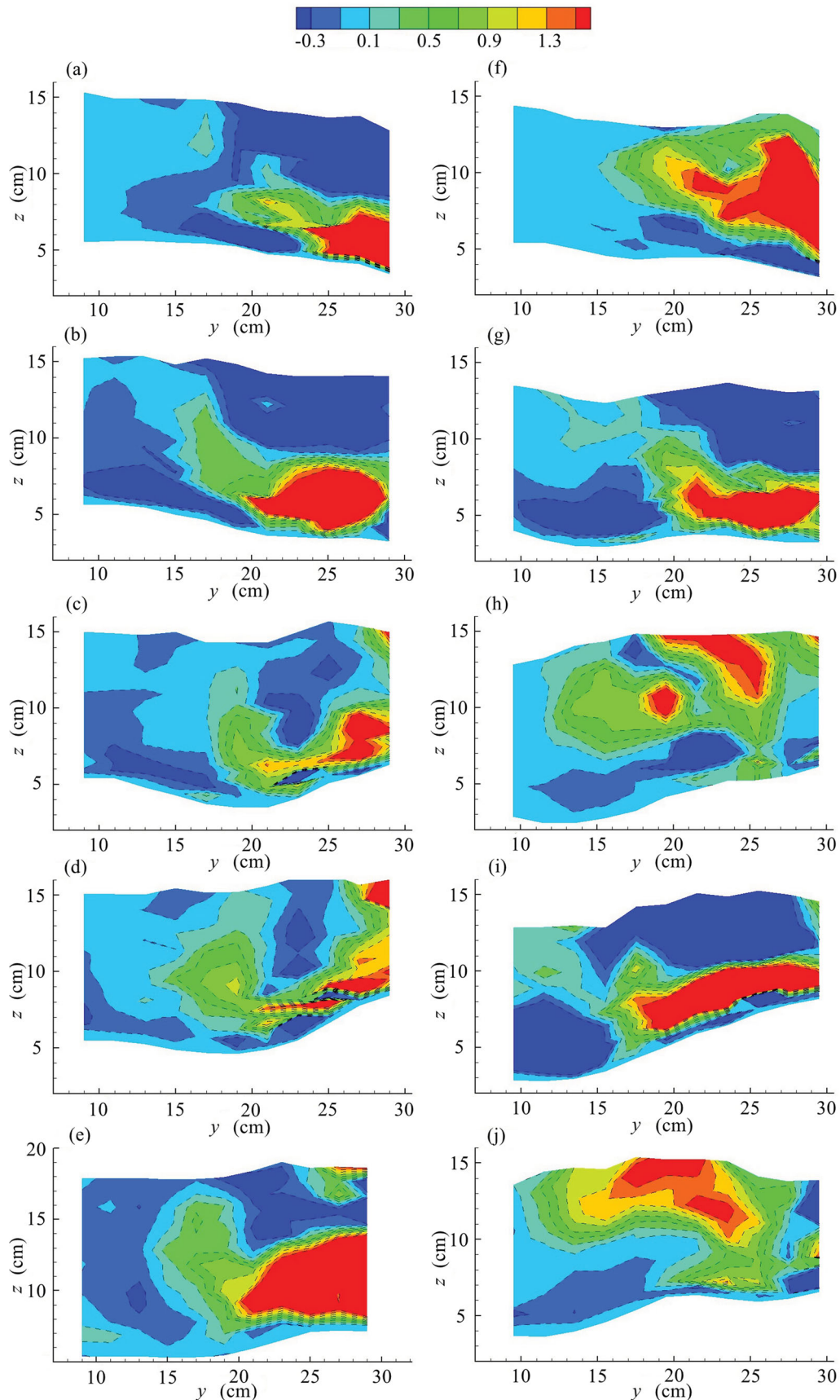


Figure 10 Patterns of the Reynolds shear stress  $\langle v'w' \rangle$  (units:  $\text{cm}^2 \text{s}^{-2}$ ) of two cases (Table 1), with (a–e) representing five cross sections S1–S5, respectively; and (f–j) representing C1–C5, respectively

(e.g. Best, 1987, 1988; Borghei & Sahebari, 2010; Guillén-Ludeña et al., 2015; Leite Ribeiro et al., 2012; Rhoads & Kenworthy, 1995, 1998; Rhoads et al., 2009).

Best (1987) proposed a conceptual model for flow dynamics at channel confluences, which consisted of six distinct regions of flow stagnation, flow deflection, flow separation, maximum velocity, gradual flow recovery and the shear layer. In this study, a region of low-velocity flow is observed between the shear layer and the region of maximum-velocity flow in the case of a small discharge ratio, which has not been reported before. The widening of the post-confluence channel can reduce the acceleration of the flow originating from the tributary, resulting in the formation of the region of low-velocity flow. In addition, the maximum-velocity flow is not as pronounced as that reported by Best (1987), which may also be due to the widening of the post-confluence channel. However, this influence can be decreased when the tributary has a larger discharge. The region of maximum velocity flow is near the inner bank, and flow velocities decrease gradually into the outer bank. However, the other regions, such as the regions of flow deflection, flow separation, flow recovery and the shear layer, can be observed in both cases.

Helical flows characterized by increased turbulence levels (Fig. 7) and Reynolds shear stress  $\langle v'w' \rangle$  (Fig. 10) are located near the bed surface, which involve the downwelling flow pointing to the mid-channel scour hole and the upwelling flow along the avalanche face of the bank-attached bar. Some previous studies have proposed that such cells appear to be responsible for scour formation as a result of depression of the core of maximum velocity and/or intense shear towards the bed by downwelling flow (e.g. Ashmore, 1982; Ashmore, Ferguson, Prestegaard, Ashworth, & Paola, 1992; Bridge, 1993). However, in this study, the core of the maximum velocity is far away from the scour hole in both cases, and helical flow cells are coincident with the corridor of the sediment on the avalanche face of the bar. Hence, the formation of the mid-stream scour hole and the lateral bar shall result from these helical flow cells. Best (1987, 1988) suggested that the counter-rotating helical vortices, which were flow-separation cells in the lee of each avalanche face, resulted from scouring and contributed to further segregate bed-load transport on each side of the scour and thus maintenance of the deep scour. However, these leeside eddies are not observed in this study.

The shear layer is an important feature of open-channel confluences, and it is characterized by increased turbulence levels (Fig. 7). The development of eddies within the shear layer is similar to that of traditional vortex pairing, leading to substantial lateral transfer of fluid between the two combining flows (Rhoads & Sukhodolov, 2001; Sukhodolov & Rhoads, 2001). These quasi-two-dimensional vortices driven by the Kelvin–Helmholtz instability could be identified by energy spectra, and especially when the spectra of transverse velocities for the shear layer near the water surface exhibit a characteristic “hump” at a low frequency (Rhoads & Sukhodolov, 2004; Yuan et al., 2016).

Sometimes, the shear layer can be populated by quasi two-dimensional eddies with opposing sense of rotation when the discharges of two rivers are comparable (Constantinescu et al., 2012). The location of the shear layer can be determined more precisely by the large values of  $\langle u'v' \rangle$ , which are related to the two-dimensional horizontal motions caused by vortices with near vertical axes, rather than by the turbulent kinetic energy (Rhoads & Sukhodolov, 2008). The shear layer at open channel confluences with a small width-to-depth ratio can easily be distorted, especially at the urban channel confluences with a large discharge ratio (Figs 6 and 7; Yuan et al., 2016). Yuan et al. (2016) presented that the flow structure and turbulence in the distorted shear layer on an unmovable bed could result in the redistribution of the maximum turbulent kinetic energy and Reynolds shear stress, which can also be observed on the degraded bed in this study (Figs 7–10). However, the highly degraded bed makes the flow structure and turbulence more complex. In this study, the distorted shear layer that accounts for about 1/3 of the whole cross section can be intensified or even truncated by the bulged bed morphology. Moreover, the bed morphology in the case of a large discharge ratio intensifies the transverse gradient of flow velocities, resulting in an increase of turbulence. Best (1987) believed that the shear layer with powerful vertical vortices, together with the increase of flow velocity, could result in an increase in bed shear stresses within the junction and considerable bed scour. However, in this study, the shear layer deviates from the scour hole, and there are no maximum flow velocities and no strong turbulence at the scour hole, especially when the discharge of the tributary is large. These results suggest that the shear layer shall not be responsible for the deep scour hole. The similar conclusion was made by Sukhodolov and Rhoads (2001) that although the shear layer was in general located within the scour-hole area, it did not necessarily imply that the shear-layer turbulence generated scouring. In line with Rhoads et al. (2009), we believe that helical motions contribute to the scour at channel confluences. The intense shear towards the bed by downwelling flow involved in the helical cells is responsible for sediment entrainment; and the upwelling flow is responsible for the sediment conveyance along the avalanche face of the bar, thereby promoting the mid-channel scour hole.

Sediment continuity requirements can explain the morphology in the reported experiments, including the development of a bank-attached lateral bar, a corner deep scour hole and a mid-channel deep scour hole adjacent to the bar. The corner deep scour hole with vertical vortices is similar to the bridge scour formed by the removal of sediment from around bridge piers. This corner scour has also been reported by Borghei and Sahebari (2010). However, it may disappear sometimes, and avalanche faces form at the mouth of each confluent channel and often slope into the mid-channel scour hole (Best, 1988). In this study, there is a significant difference in the flow structures above the mid-channel scour hole between the two cases. When the tributary discharge is low, the scour hole is located

at the inner edge of the shear layer where the low-velocity flow, the maximum positive horizontal-vertical cross stresses, and the strong downwelling flow are located. However, when the tributary discharge is high, the shear layer is deflected far away from the hole. A strong downwelling flow is observed, but with no pronounced turbulence. The scour hole is responding to the increased penetration of the tributary fluid into the junction at the higher discharge ratio (Best, 1988; Mosley, 1976). The thalweg of the scour hole tends to be parallel to the bank when the discharge ratio is large. Sometimes, the mid-channel scour hole is limited at river confluences with a moderate bed discordance, dominant sediment supply by the tributary, lower junction angles or bed material that imparts a high relative roughness (Boyer et al., 2006; De Serres et al., 1999; Roy, Roy, & Bergeron, 1988). Two sand ridges are observed with the maximum height located at the downstream of the bank-attached bar, resulting in the formation of two small depressions. One depression is located adjacent to the inner bank and the other one is located between the two sand ridges, corresponding to the corridors for the transport of sediment eroded from the two scour holes. However, these two sand ridges are merged to form a post-confluence mid-channel bar because the water velocities, as well as the turbulence intensities, decrease as the flows recover (Rhoads & Sukhodolov, 2004; Sukhodolov & Rhoads, 2001).

Leite Ribeiro et al. (2012) and Guillén-Ludeña et al. (2015, 2016) have conducted laboratory experiments to investigate the hydro-morphodynamics at a 90° channel confluence. Unlike the clear-water condition with no sediment supply in this study, the sediment was supplied to the main channel in the study of Leite Ribeiro et al. (2012) and to both channels in the study of Guillén-Ludeña et al. (2015). In line with our study, they also observed a bank-attached bar at the downstream of the confluence and a mid-stream scour hole. Additionally, they observed the avalanche slope at the tributary mouth and the discordance between the tributary and the main channel, which should be associated with the supply of sediment to the tributary. The sediment supplied to the main channel contributed to maintain the texture of the sediment mixture (Guillén-Ludeña et al., 2015), but an armour layer could form after the erosion of finer particles if no sediment was supplied (this study; Leite Ribeiro et al., 2012). The corner scour hole observed in this study was also observed in the initial stage by Guillén-Ludeña et al. (2015), but it was soon filled by the migrating wedge originating from the tributary. Sediment segregation was evident in the study of Leite Ribeiro et al. (2012) and Guillén-Ludeña et al. (2015), so that the finer sediment originating from the tributary moved through the corridor along the inner bank and the coarser sediment moved along the slope face of the bar, and the sediment originating from the main channel moved along the outer bank. In this study, different patterns of sediment transport are observed. The sediment eroded from the corner scour hole is transported along the face of the inner ridge, and finer sediment could be lifted over the inner ridge and then transported in the inner corridor. However, the sediment eroded from the other scour hole

is transported along the face of the outer ridge. Then, finer sediment can be lifted over the outer ridge and then transported in the corridor between the two ridges, and coarser sediment is left to armour the bed surface. In the case of a larger tributary discharge, a larger amount of sediment is eroded, thereby producing a deeper scour hole (Guillén-Ludeña, Franca, Cardoso, & Schleiss, 2016), and coarse sediment can settle down to form a post-confluence mid-channel bar. However, this was not observed by Leite Ribeiro et al. (2012) and Guillén-Ludeña et al. (2015). As a result, the total amount for erosion in this case is limited, and the sediment deposited in the mid-channel bar is coarser than that at the bank-attached bar (Best 1988). There is an obvious sorting of sediment on the degraded bed surface with a high percentage of fine grains at the bar and a high percentage of coarse grains at the deep hole, respectively. There is also an obvious sorting of sediment on the face of the bar, and the diameter of sediment increases from the top toward the toe of the bar face in the scour hole, which was also observed by Leite Ribeiro et al. (2012) and Guillén-Ludeña et al. (2015). Rhoads et al. (2009) observed similar bed morphology consisting of an outer-bank scour hole and an inner-bank bar, and evident sorting of sediment on the face of the bar in the field, particularly for the high discharge-ratio conditions. In addition, the dual surface-convergent helical cells played a critical role in sediment transport and bed morphology when the discharges of two combining channels were comparable. However, these dual surface-convergent helical cells were not observed in this study, probably due to the different discharges of two combining channels in our laboratory experiment.

## 6 Conclusions

Several important conclusions can be drawn from this study:

- (1) The bed morphology at an artificial channel confluence is characterized by a bank-attached lateral bar, a deep scour hole at the corner, a mid-channel deep scour hole adjacent to the bar, and two sand ridges that correspond to the corridors of sediment transport is observed at open channel confluences. Confluent flows with a large discharge ratio can produce more pronounced bed morphology such as a larger dimension of mid-stream scour hole than a small discharge ratio.
- (2) A region of low-velocity flow is observed between the shear layer and the region of maximum-velocity flow when the discharge ratio is small, but disappears when the discharge ratio is large. The origin of this region contributes to the widening of the post-confluence channel.
- (3) A helical cell characterized by increased turbulence levels and positive values of  $\langle v'w' \rangle$  is located near the bed surface, which involves the downwelling flow to the mid-channel scour hole and the upwelling flow along the avalanche face of the bank-attached bar. The spatial evolution of

- dimensions and intensities can be influenced significantly by different discharge ratios.
- (4) The shear layer characterized by increased turbulence levels and positive values of  $\langle u'v' \rangle$  and  $\langle u'w' \rangle$  is located in the outer side of the scour hole when the discharge ratio is small, and tends to be distorted and intensified or even truncated by the bulged bed morphology in the case of a large discharge ratio.
  - (5) The downwelling flow and upwelling flow involved in helical motions, associated with the intense shear to the bed, are responsible for sediment entrainment and scouring, thereby producing and promoting the mid-channel scour hole.

The present research on urban channel confluences is based on laboratory experiments which have limitations reproducing all aspects of reality. In the future, field investigation of urban channel confluences should be envisaged to compare with the present results.

### Acknowledgements

The authors would like to thank Huiming Zhang and Guolong Zhao of Hohai University for assistance during the experiments. Thanks are also extended to Professor Bidya Sagar Pani of the Indian Institute of Technology Bombay for help in revising this work. The paper was considerably improved thanks to the comments and suggestions of the Editor and reviewers.

### Funding

This work was partly supported by National Science Foundation of China [grant numbers 51239003, 51509073, 51279046], and the Fundamental Research Funds for the Central Universities, the Ministry of Education of the People's Republic of China [grant number 2017B11214].

### Notation

$B$	= channel width (m)
$d$	= sediment diameter (m)
$d_x$	= diameter for which $x\%$ of the sediment is finer (m)
$F$	= Froude number (—)
$h$	= water depth (m)
$k$	= turbulent kinetic energy ( $\text{m}^2 \text{s}^{-2}$ )
$n$	= number of velocity data (—)
$Q$	= discharge ( $\text{m}^3 \text{s}^{-1}$ )
$\gamma$	= discharge ratio (—)
$R$	= Reynolds number (—)
$u, v, w$	= velocity components ( $\text{m s}^{-1}$ )
$u', v', w'$	= fluctuating velocity components ( $\text{m s}^{-1}$ )
$u_i$	= velocity components ( $\text{m s}^{-1}$ )
$\langle u_i \rangle$	= mean value of velocity ( $\text{m s}^{-1}$ )

$\langle u_i'^2 \rangle$	= turbulent kinetic energy of fluctuating velocity components ( $\text{m}^2 \text{s}^{-2}$ )
$x, y, z$	= streamwise, lateral and vertical coordinate (m)
$\rho$	= water density ( $\text{kg m}^{-3}$ )
$\sigma$	= sorting coefficient (—)

### Subscripts

$t$	= tributary
$m$	= main channel
$pc$	= post-confluence channel

### References

- Arega, F., Lee, J. H. W., & Tang, H. (2008). Hydraulic jet control for river junction design of Yuen Long Bypass Floodway, Hong Kong. *Journal of Hydraulic Engineering*, 134, 23–33. doi:10.1061/(ASCE)0733-9429(2008)134:1(23)
- Ashmore, P. (1982). Laboratory modelling of gravel braided stream morphology. *Earth Surface Processes and Landforms*, 7, 201–225. doi:10.1002/esp.3290070301
- Ashmore, P., Ferguson, R. I., Prestegard, K. L., Ashworth, P. J., & Paola, C. (1992). Secondary flow in anabranch confluences of a braided, gravel-bed stream. *Earth Surface Processes and Landforms*, 17, 299–311. doi:10.1002/esp.3290170308
- Best, J. L. (1987). Flow dynamics at river channel confluences: Implications for sediment transport and bed morphology. In F. G. Ethridge, R. M. Flores, & M. D. Harvey (Eds.), *Recent developments in fluvial sedimentology* (pp. 27–35). Tulsa: SEPM Society for Sedimentary Geology
- Best, J. L. (1988). Sediment transport and bed morphology at river channel confluences. *Sedimentology*, 35, 481–498. doi:10.1111/j.1365-3091.1988.tb00999.x
- Best, J. L., & Reid, I. (1984). Separation zone at open-channel junctions. *Journal of Hydraulic Engineering*, 110, 1588–1594. doi:10.1061/(ASCE)0733-9429(1984)110:11(1588)
- Biron, P., Roy, A. G., & Best, J. L. (1996a). Effects of bed discordance on flow dynamics at open channel confluences. *Journal of Hydraulic Engineering*, 122, 676–682. doi:10.1061/(ASCE)0733-9429(1996)122:12(676)
- Biron, P., Roy, A. G., & Best, J. L. (1996b). Turbulent flow structure at concordant and discordant open-channel confluences. *Experiments in Fluids*, 21, 437–446. doi:10.1007/BF00189046
- Biron, P., Roy, A. G., Best, J. L., & Boyer, C. J. (1993). Bed morphology and sedimentology at the confluence of unequal depth channels. *Geomorphology*, 8, 115–129. doi:10.1016/0169-555X(93)90032-W
- Blanckaert, K. (2010). Topographic steering, flow recirculation, velocity redistribution, and bed topography in sharp meander bends. *Water Resources Research*, 46, W09506. doi:10.1029/2009WR008303

- Borghei, S. M., & Sahebari, A. J. (2010). Local scour at open-channel junctions. *Journal of Hydraulic Research*, 48, 538–542. doi:10.1080/00221686.2010.492107
- Boyer, C., Roy, A. G., & Best, J. L. (2006). Dynamics of a river channel confluence with discordant beds: Flow turbulence, bed load sediment transport, and bed morphology. *Journal of Geophysical Research-Earth Surface*, F4, F04007. doi:10.1029/2005JF000458
- Bradbrook, K. F., Lane, S. N., & Richards, K. S. (2000). Numerical simulation of three-dimensional, time-averaged flow structure at river channel confluences. *Water Resources Research*, 36, 2731–2746. doi:10.1029/2000WR900011
- Bradbrook, K. F., Lane, S. N., Richards, K. S., Biron, P., & Roy, A. G. (2000). Large eddy simulation of periodic flow characteristics at river channel confluences. *Journal of Hydraulic Research*, 38, 207–215. doi:10.1080/00221680009498338
- Bradbrook, K. F., Lane, S. N., Richards, K. S., Biron, P., & Roy, A. G. (2001). Role of bed discordance at asymmetrical river confluences. *Journal of Hydraulic Engineering*, 127, 351–368. doi:10.1061/(ASCE)0733-9429(2001)127:5(351)
- Bridge, J. S. (1993). The interaction between channel geometry water flow sediment transport and deposition in braided rivers. In J. L. Best & C. S. Bristow (Eds.), *Braided rivers* (pp. 13–72). London: Geological Society.
- Constantinescu, G., Miyawaki, S., Rhoads, B., & Sukhodolov, A. (2012). Numerical analysis of the effect of momentum ratio on the dynamics and sediment entrainment capacity of coherent flow structures at a stream confluence. *Journal of Geophysical Research-Earth Surface*, F4, F04028. doi:10.1029/2012JF002452
- Constantinescu, G., Miyawaki, S., Rhoads, B., Sukhodolov, A., & Kirkil, G. (2011). Structure of turbulent flow at a river confluence with momentum and velocity ratios close to 1: Insight provided by an eddy resolving numerical simulation. *Water Resources Research*, 5, W05507. doi:10.1029/2010WR010018
- De Serres, B., Roy, A. G., Biron, P., & Best, J. L. (1999). Three-dimensional structure of flow at a confluence of river channels with discordant beds. *Geomorphology*, 26, 313–335. doi:10.1016/S0169-555X(98)00064-6
- Ferguson, R., & Hoey, T. (2008). Effects of tributaries on main-channel geomorphology. In S. P. Rice, A. G. Roy, & B. L. Rhoads (Eds.), *River confluences, tributaries and the fluvial network* (pp. 183–208). Chichester: John Wiley & Sons.
- Goring, D. G., & Nikora, V. I. (2002). Despiking acoustic Doppler velocimeter data. *Journal of Hydraulic Engineering*, 128, 117–126. doi:10.1061/(ASCE)0733-9429(2002)128:1(117)
- Guillén-Ludeña, S., Franca, M. J., Cardoso, A. H., & Schleiss, A. J. (2015). Hydro-morphodynamic evolution in a 90° movable bed discordant confluence with low discharge ratio. *Earth Surface Processes and Landforms*, 40, 1927–1938. doi:10.1002/esp.3770
- Guillén-Ludeña, S., Franca, M. J., Cardoso, A. H., & Schleiss, A. J. (2016). Evolution of the hydromorphodynamics of mountain river confluences for varying discharge ratios and junction angles. *Geomorphology*, 255, 1–15. doi:10.1016/j.geomorph.2015.12.006
- Kumar, A., & Kothyari, U. C. (2012). Three-dimensional flow characteristics within the scour hole around circular uniform and compound piers. *Journal of Hydraulic Engineering*, 138, 420–429. doi:10.1061/(ASCE)HY.1943-7900.0000527
- Leite Ribeiro, M. L., Blanckaert, K., Roy, A. G., & Schleiss, A. J. (2012). Flow and sediment dynamics in channel confluences. *Journal of Geophysical Research-Earth Surface*, F1, F01035. doi:10.1029/2011JF002171
- Lemmin, U., & Rolland, T. (1997). Acoustic velocity profiler for laboratory and field studies. *Journal of Hydraulic Engineering*, 123, 1089–1098. doi:10.1061/(ASCE)0733-9429(1997)123:12(1089)
- Liriano, S. L., Day, R. A., & White, W. R. (2002). Scour at culvert outlets as influenced by the turbulent flow structure. *Journal of Hydraulic Research*, 40, 367–376. doi:10.1080/00221680209499951
- Mosley, P. (1976). An experimental study of channel confluences. *The Journal of Geology*, 84, 535–562. Retrieved from <http://www.jstor.org/stable/30066212>
- Rhoads, B. L., & Kenworthy, S. T. (1995). Flow structure at an asymmetrical stream confluence. *Geomorphology*, 11, 273–293. doi:10.1016/0169-555X(94)00069-4
- Rhoads, B. L., & Kenworthy, S. T. (1998). Time-averaged flow structure in the central region of a stream confluence. *Earth Surface Processes and Landforms*, 23, 171–191. doi:10.1002/(SICI)1096-9837(199802)23:2<171::AID-ES\_P842>3.0.CO;2-T
- Rhoads, B. L., Riley, J. D., & Mayer, D. R. (2009). Response of bed morphology and bed material texture to hydrological conditions at an asymmetrical stream confluence. *Geomorphology*, 109, 161–173. doi:10.1016/j.geomorph.2009.02.029
- Rhoads, B. L., & Sukhodolov, A. N. (2001). Field investigation of three-dimensional flow structure at stream confluences: part I. Thermal mixing and time-averaged velocities. *Water Resources Research*, 9, 2393–2410. doi:10.1029/2001WR000316
- Rhoads, B. L., & Sukhodolov, A. N. (2004). Spatial and temporal structure of shear-layer turbulence at a stream confluence. *Water Resources Research*, 6, 2393–2410. doi:10.1029/2003WR002811
- Rhoads, B. L., & Sukhodolov, A. N. (2008). Lateral momentum flux and the spatial evolution of flow within a confluence mixing interface. *Water Resources Research*, 44, 27–143. doi:10.1029/2007WR006634
- Rolland, T. (1994). *Développement d'une instrumentation Doppler ultrasonore adaptée à l'étude hydraulique de la turbulence dans les canaux (Unpublished doctoral dissertation)*. EPFL, Lausanne, Switzerland.

- Roy, A. G., Roy, R., & Bergeron, N. (1988). Hydraulic geometry and changes in flow velocity at a river confluence with coarse bed material. *Earth Surface Processes and Landforms*, 13, 583–598. [doi:10.1002/esp.3290130704](https://doi.org/10.1002/esp.3290130704)
- Sukhodolov, A. N., & Rhoads, B. L. (2001). Field investigation of three-dimensional flow structure at stream confluences: 2. Turbulence. *Water Resources Research*, 37, 2411–2424. [doi:10.1029/2001WR000317](https://doi.org/10.1029/2001WR000317)
- Vanoni, V. A. (Ed.). (1975). *Sedimentation Engineering*. New York, NY: American Society of Civil Engineers.
- Yang, Q., Wang, X., Lu, W., & Wang, X. (2009). Experimental study on characteristics of separation zone in confluence zones in rivers. *Journal of Hydrologic Engineering*, 2, 166–171. [doi:10.1061/\(ASCE\)1084-0699\(2009\)14:2\(166\)](https://doi.org/10.1061/(ASCE)1084-0699(2009)14:2(166))
- Yuan, S., Li, L., Amini, F., & Tang, H. (2014). Turbulence measurement of combined wave and surge overtopping of a full-scale HPTRM-strengthened levee. *Journal of Waterway, Port, Coastal, and Ocean Engineering*, 140, 04014014. [doi:10.1061/\(ASCE\)WW.1943-5460.0000230](https://doi.org/10.1061/(ASCE)WW.1943-5460.0000230)
- Yuan, S., Tang, H., Xiao, Y., Qiu, X., Zhang, H., & Yu, D. (2016). Turbulent flow structure at a 90-degree open channel confluence: accounting for the distortion of the shear layer. *Journal of Hydro-environment Research*, 12, 130–147. [doi:10.1016/j.jher.2016.05.006](https://doi.org/10.1016/j.jher.2016.05.006)